processes

MDPI

Article

Experimental Evaluation on the Catalytic Activity of a Novel CeZrK/rGO Nanocomposite for Soot Oxidation in Catalyzed Diesel Particulate Filter

Gang Wu [1], Ke Tang [1], Deng Wu [1], Yuelin Li [1] and Yuqiang Li [2,*]

[1] College of Automotive and Mechanical Engineering, Changsha University of Science and Technology, Changsha 410114, China; wugang@csust.edu.cn (G.W.); ke137359824@163.com (K.T.); m15073184778@163.com (D.W.); li.yuelin@163.com (Y.L.)
[2] School of Energy Science and Engineering, Central South University, Changsha 410083, China
* Correspondence: csulyq@csu.edu.cn

Abstract: A nanostructured solid solution catalyst CeZrK/rGO for soot oxidation in catalyzed diesel particulate filter was synthesized using the dipping method. The reduced graphene oxide (rGO) was used as the catalyst carrier, and CeO_2, ZrO_2, and K_2O were mixed with the molar ratio of 5:1:1, 5:2:2 and 5:3:3, which were referred to as $Ce_5Zr_1K_1$/rGO, $Ce_5Zr_2K_2$/rGO, and $Ce_5Zr_3K_3$/rGO, respectively. The structure, morphology and catalytic activity of the CeZrK/rGO nanocomposites were thoroughly investigated and the results show that the CeZrK/rGO nanocomposites have nanoscale pore structure (36.1–36.9 nm), high-dispersion quality, large specific surface area (117.2–152.4 m^2/g), small crystallite size (6.7–8.3 nm), abundant oxygen vacancies and superior redox capacity. The 50% soot conversion temperatures of $Ce_5Zr_1K_1$/rGO, $Ce_5Zr_2K_2$/rGO, and $Ce_5Zr_3K_3$/rGO under tight contact condition were decreased to 352 °C, 339 °C and 358 °C respectively. The high catalytic activity of CeZrK/rGO nanocomposites can be ascribed to the following factors: the doping of Zr and K ions causes the nanocrystalline phase formation in CeZrK solid solutions, reduces the crystallite size, generates abundant oxygen vacancies and improves redox capacity; the rGO as a carrier provides a large specific surface area, thereby improving the contact between soot and catalyst.

Keywords: soot oxidation; reduced graphene oxide; solid solution catalyst; catalytic activity; catalyzed diesel particulate filter

Citation: Wu, G.; Tang, K.; Wu, D.; Li, Y.; Li, Y. Experimental Evaluation on the Catalytic Activity of a Novel CeZrK/rGO Nanocomposite for Soot Oxidation in Catalyzed Diesel Particulate Filter. *Processes* **2021**, *9*, 674. https://doi.org/10.3390/pr9040674

Academic Editor: Zhihua Wang

Received: 15 March 2021
Accepted: 8 April 2021
Published: 12 April 2021

1. Introduction

The diesel engine has been widely used in transportation and various non-road construction machinery due to a high thermal efficiency [1]. However, its exhausted emissions can cause serious environmental pollution and endanger human health at the same time, especially for soot which can enter the blood, trigger genetic mutations and create health risks [2,3]. In recent years, with the increasingly stringent emission regulations, the control technologies of the soot emission in diesel engines have become the focus of governments and scholars of various countries [4].

In the current scenario, soot is mainly caused by the incomplete combustion of hydrocarbon compounds inside the engine under high temperature and oxygen deficiency. In the post-treatment system, it gets into contact with the catalyst and reacts at high temperatures to form CO_2. Diesel particulate filter (DPF) is an effective tool to control soot from diesel engine. Generally, the exhaust temperature ranges from 150 °C to 450 °C, while the oxidation temperature of soot exceeds 550 °C. It is, therefore, necessary to raise the temperature for soot combustion, but excessive soot combustion temperature will damage the filter material [5]. Therefore, a superior solution is to reduce the oxidation reaction temperature of soot using catalysts. Catalyzed diesel particulate filter (CDPF) does not need an extra heat source and complex control system, and thus it greatly reduces fuel consumption

and engine cost. As the catalytic oxidation of soot is a reaction between O_2, soot and the catalyst, the contact between soot and the catalyst and the activity of the catalyst are two key factors affecting the soot oxidation efficiency [6], which is a critical issue in CDPF regeneration. Accordingly, the design and preparation of catalysts with large contact area and high intrinsic activity are significant for the CDPF.

The noble metal catalysts have a superior intrinsic catalytic activity, but the price is too expensive, limiting their applications in CDPF [7]. It was established that the oxides of rare earth metal, like $Ce_{0.5}Zr_{0.5}O_2$ [8], $LaFeO_3$ [9], $LaMn_{0.8}Pt_{0.2}O_3$ [10], can catalyze the oxidation of soot. Among them, CeO_2 presents superior oxygen storage capacity (OSC) and catalytic performance over other traditional metal oxide catalysts in oxidizing soot at low temperature [11]. The introduction of external cations can cause the lattice distortion of CeO_2 and increase oxygen vacancies, improving the redox capacity and catalytic activity of CeO_2 [12]. It was reported by Atribak et al. [13] and Gross et al. [14] that the addition of Zr and K ions can enhance high-temperature stability and oxygen storage capacity of the catalysts, respectively. Thus, it can be inferred that the doping of these two elements in the catalyst can improve soot oxidation.

It is important to select a suitable substrate to increase the surface area, improve adsorption and provide more active sites on the catalyst. Graphene exists as a 2D nanomaterial with a honeycomb hexagonal structure composed of Sp^2 hybridized carbon atoms (Olabi et al., 2020). Due to excellent physical and chemical properties, graphene has attracted extensive attention. The super-large specific surface area and special pore structure of graphene enable the metal nanoparticles loaded onto graphene to get a good dispersion, thus ensuring sufficient contact area between the active components of the catalyst and soot. Tan et al. [15] found that the maximum adsorption capacity of NiAl-LDH/rGO composite with a sandwich structure toward uranium is up to 277.8 mg/g. The high adsorption capacity has to do with the specific surface area and special pore structure characteristics of rGO. Due to the negatively charged nature of graphene and positively charged nature of the metal cation, the combination between rGO and metal oxide particles can be easily achieved by electrostatic interaction, which is conducive to the uniform dispersion of metal oxide particles on rGO [16]. Some researchers have pointed out that graphene-based materials can stabilize active sites and inhibit surface migration of metal nanoparticles, guaranteeing high catalytic stability even under severe operating conditions [17–19]. Therefore, the usage of graphene as the matrix of catalysts is a feasible strategy.

Still, the weak thermal-oxidative stability of bare graphene makes it easy to decompose during combustion. This impact is negative on the catalytic activity. Consequently, intellectual capital and resources are being committed to upturn the thermal stability of graphene by surface modification. Generally speaking, modified graphene is to compound other substances with active components through covalent or non-covalent interactions so that graphene has other special properties while maintaining its original properties [20]. Li et al. [21] portrayed that zirconium phosphate nanoparticles immobilized on the surface of graphene oxide (GO) yielded superior thermal stability and flame retardancy to the phenolic foams, and this is essentially ascribed to the harmonious impacts of zirconium phosphate nanoparticles and GO. Wu et al. [22] prepared graphene sheets using the hydrogen arc discharge exfoliation method. The materials exhibit a remarkable thermal stability from GO with an oxidization resistance temperature of 601 °C. The research performed by Bora et al. [23], Yuan et al. [24] and Zong et al. [25] found that rGO exhibited a higher thermal stability than GO due to the removal of thermally labile oxygen functional groups during the reduction process. Salavagione et al. [4] report a strategy for the synthesis of vinylalcohol/rGO nanocomposites and found the thermal stability was improved by more than 100 °C.

This study aims to develop a catalyst with high catalytic activity, i.e., CeO_2-ZrO_2-K_2O/rGO (referred to as CeZrK/rGO), for soot oxidation in the CDPF. The structure and morphology of the catalyst were thoroughly characterized using field emission scanning electron microscopy (FESEM), transmission electron microscopy (TEM), N_2 adsorption-

desorption tests, X-ray powder diffraction (XRD), X-ray photoelectron spectroscopy (XPS), Fourier transform infrared spectrometry (FTIR), Raman spectra and H_2-temperature programmed reduction (TPR) methods. The catalytic performance of the catalyst was evaluated using thermogravimetric analysis.

2. Experimental Methods

2.1. Catalyst Preparation

The schematic diagram of the catalyst's preparation process is shown in Figure 1. All materials were of analytical grade and used without further purification. Graphene oxide was prepared by the Hummer method in the oxidation-reduction method [26]. Under low temperature stirring conditions, some amount of concentrated sulfuric acid and strong oxidant were sequentially added to the graphite powder, diluted with water and hydrogen peroxide, heated and dried, and then subjected to ultrasound exfoliation to obtain graphene oxide. $Ce(NO_3)_3{\cdot}6H_2O$, $ZrO(NO_3)_2{\cdot}6H_2O$, and KNO_3 were dissolved in deionized water by magnetic stirring to generate the salt solution containing the metallic ions of Ce, Zr, and K. Then, 60 mg of GO was put into 30 mL of deionized water to generate the GO solution under the ultrasonic treatment for 0.5 h. The prepared solutions were mixed and then processed by the ultrasonic treatment for 0.5 h. The mixed solution was heated in a water bath at 80 °C for 1 h. Ammonia hydroxide was added into the heated solution and gently stirred until pH 10 ± 0.1 was reached. The obtained solution was hydrothermally treated at 160 °C for 12 h. After that, the solution was washed with deionized water by repeated centrifugations until the pH was adjusted to neutral. The solution was further freeze-dried for 18 h in a FD-1A-80 vacuum freeze drier to obtain the precursor. It was calcined at 200 °C for 2 h in a tube furnace under argon atmosphere to realize CeZrK/rGO.

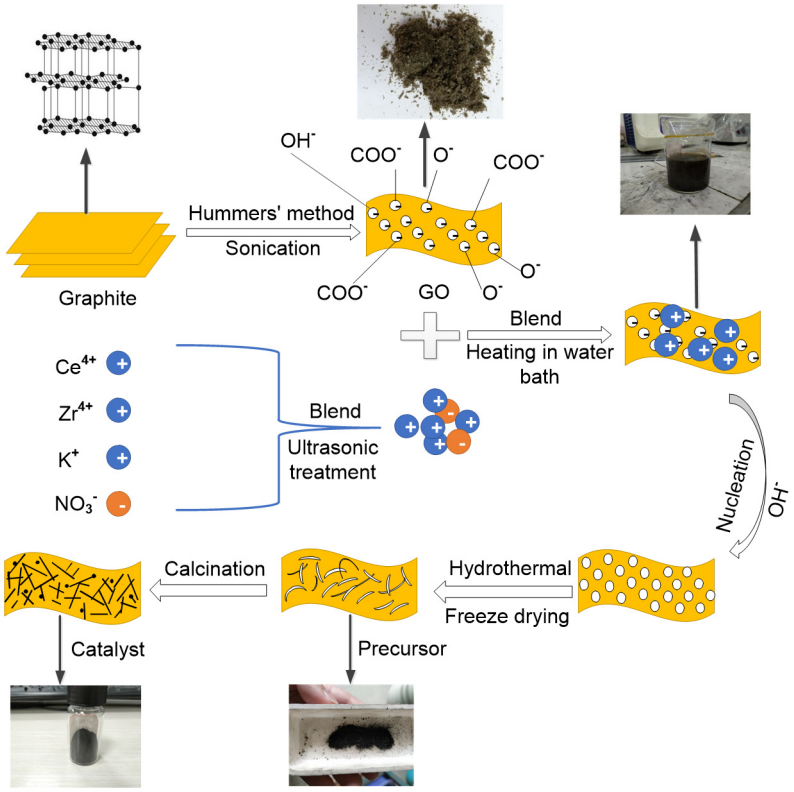

Figure 1. Schematic diagram of CeZrK/rGO catalysts preparation.

2.2. Experimental Apparatus

The morphology and composition of catalysts were investigated by FESEM (Czech Nova NanoSEM 230, FEI Company, Hillsboro, OR, USA) equipped with energy dispersive X-ray (EDX). The TEM images were acquired by an FEI Tecnai G2 F20 at an accelerating

voltage of 200 kV. The crystal structure of the catalysts was observed using a Rigaku D/Max 2550 XRD (Tokyo, Japan). The static adsorption and desorption tests were carried out on a Micromeritics ASAP2020 to obtain N_2 adsorption/desorption isotherms. The specific surface area and the pore size distribution were calculated from the adsorption branch and desorption branch of the isomers based on Brunauer-Emmett-Teller (BET) and Barrett-Joyner-Halenda (BJH) methods, respectively. The XPS spectra was recorded on an ESCALAB 250Xi XPS in the analysis chamber of 2×10^{-9} Pa using Al Kα radiation (1486.6 eV), and the obtained binding energies were referenced to C 1s line set at 284.9 eV. The FT-IR spectra was obtained on a Nicolet iS50 FT-IR (Thermo Fisher Scientific, Waltham, MA, USA) using potassium bromide (KBr) beamsplitter. The Raman spectra were measured using a Horiba Jobin-Yvon HR800 Raman spectrometer (Kyoto, Japan) with a 532 nm line of Ar^+ ion laser as the excitation source at room temperature. The TG 209 F3 Tarsus (Netzsch, Selb, Germany) was used to carry out the thermogravimetric analysis, under the temperature range between room temperature and 900 °C with a heating rate of 10 °C·min^{-1}. The TPR measurements were carried out on an Auto Chem II 2920 instrument equipped with a thermal conductivity detector (TCD). Each time, 40 mg of the sample was heated from room temperature to 800 °C at a heating rate of 10 °C·min^{-1}. A mixed gas consisting of 10% H_2 in Ar at a fixed flow rate of 20 mL·min^{-1} was used as reductant.

In the experiment, the soot and the cerium-based catalyst were mixed in loose contact and close contact, respectively. In close contact conditions, the soot particles and the catalyst powder were mixed and ground in an agate mortar for 30 min. In loose contact conditions, a stainless-steel spatula is used to uniformly mix soot particles with the same mass ratio and catalyst powder for 3–4 min. Under the two working conditions, the masses of soot and cerium-based catalyst in the crucible were 4 mg and 40 mg. A thermogravimetry technique using Printex-U soot (Degussa, Frankfurt, Germany) as the model reactant was utilized to assess the catalytic soot activity of the catalysts. The catalytic activity of the catalysts for diesel soot combustion were realized using simulated air (21% O_2 + 79% N_2) or pure N_2 under different contact modes. The thermogravimetric analysis was performed in a TG 209 F3 Tarsus under the temperature range between room temperature and 650 °C with a heating rate of 10 °C·min^{-1}.

3. Results and Discussion

3.1. Characterization Studies

The SEM and TEM techniques were employed to characterize the morphology and size of the catalysts as shown in Figure 2a,c,e and Figure 2b,d,f, respectively. It can be seen from Figure 2a that the substrate material of graphene exists in the form of a translucent sheet with wrinkles and folds. Looking at Figure 2c,e, it is apparent that metal oxide particles are uniformly and highly dispersed on graphene. It can be found from TEM images that $Ce_5Zr_2K_2$/rGO presents the most evenly dispersed metal oxide particles compared to $Ce_5Zr_1K_1$/rGO and $Ce_5Zr_3K_3$/rGO. By using Nano measurer software [27], the average particle size of $Ce_5Zr_1K_1$/rGO, $Ce_5Zr_2K_2$/rGO, and $Ce_5Zr_3K_3$/rGO were 9.65 nm, 7.42 nm, and 9.39 nm, respectively, which were smaller than that of $CeZrO_x$ catalysts (15–20 nm) [28]. It has been shown that graphene inhibits the surface migration of metal oxide nanoparticles and reduces the size of metal oxide nanoparticles [29].

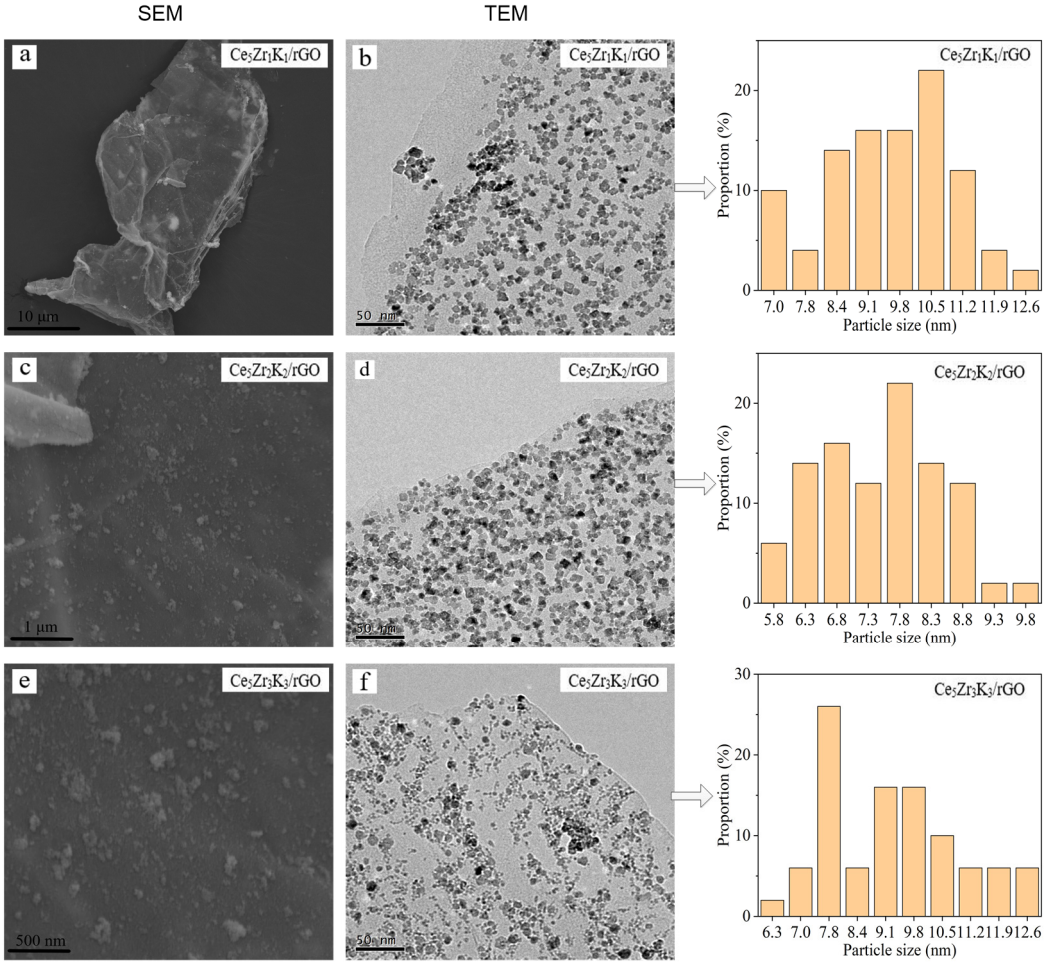

Figure 2. Scanning electron microscopy (SEM) and transmission electron microscopy (TEM) images of CeZrK/rGO catalysts.

To obtain the distributed information of Ce, Zr, and K elements in the $Ce_5Zr_2K_2$/rGO catalysts, the EDX elemental mapping is shown in Figure 3. The catalysts presented a uniform and orderly element distribution, and elements Ce, Zr, K, C, and O were highly dispersed on the catalysts [19]. It can be further verified in TEM images that the rGO carrier was loaded with well-dispersed spherical metal oxide nanoparticles. The catalytic oxidation of soot belonged to the heterogeneous catalytic reaction, and thus the contact between soot and catalyst was one of the most important influencing factors on the catalytic activity and efficiency. Therefore, the well-dispersed metal oxide nanoparticles promoted the catalytic oxidation of soot.

The XRD patterns of CeO_2 and $Ce_5Zr_2K_2$/rGO catalysts are depicted in Figure 4. It was observed that all the catalysts show a typical cubic structured CeO_2 peak. The XRD of CeZrK/rGO catalysts showed a series of reflections at 29° (111), 33° (200), 47° (220), 56° (331), 59° (222) and 69° (400) indexed to typical cubic spinel CeO_2 (PDF#89-8436). The doping with Zr^{4+} and K^+ irons caused the shifting of diffraction peak towards lower angle side since Ce^{4+} was partially replaced by Zr^{4+} and K^+ ions, which led to the slight changes in cell parameter and crystallite size [30,31]. The peaks of CeZrK/rGO catalysts were wider than those of CeO_2. Meanwhile, the half-peak width of $Ce_5Zr_2K_2$/rGO was relatively wide among the CeZrK/rGO catalysts, indicating the crystallite size of $Ce_5Zr_2K_2$/rGO was smaller than that of $Ce_5Zr_1K_1$/rGO and $Ce_5Zr_3K_3$/rGO. There were no obvious characteristic diffraction peaks observed for graphene-related phases. The complete exfoliation of graphene in the hybrid was achieved as a result of efficiently avoiding the restacking of the graphene [19]. Meanwhile, no other obvious diffractions

were found in Zr-related and K-related phases, indicating that the Zr-related and K-related phases were non-crystalline states or presented as a part of CeO_2-ZrO_2-K_2O solid solution.

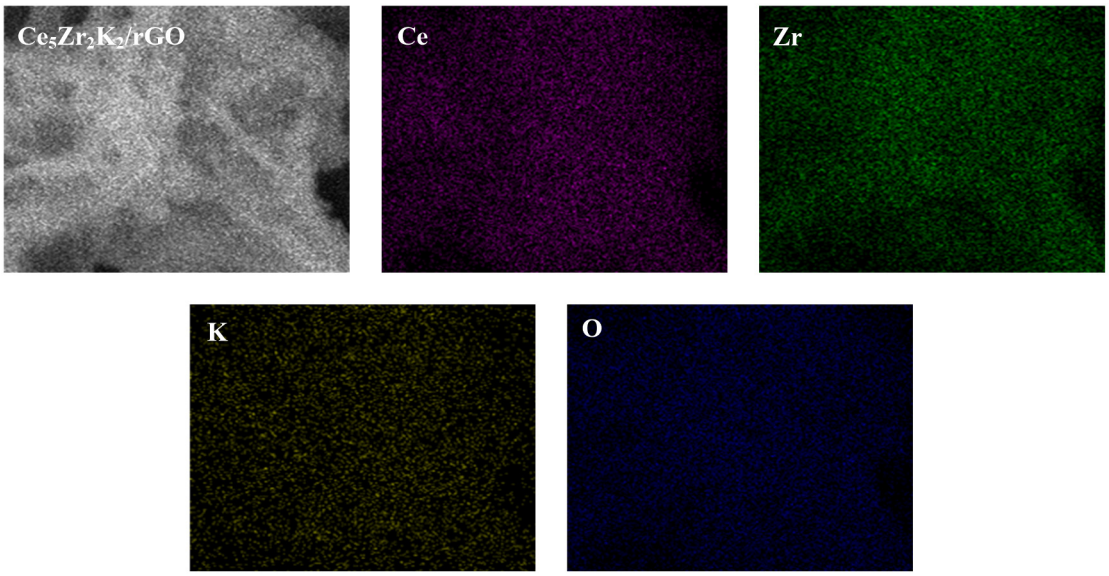

Figure 3. Energy dispersive X-ray (EDX) elemental mapping of $Ce_5Zr_2K_2$/rGO catalyst.

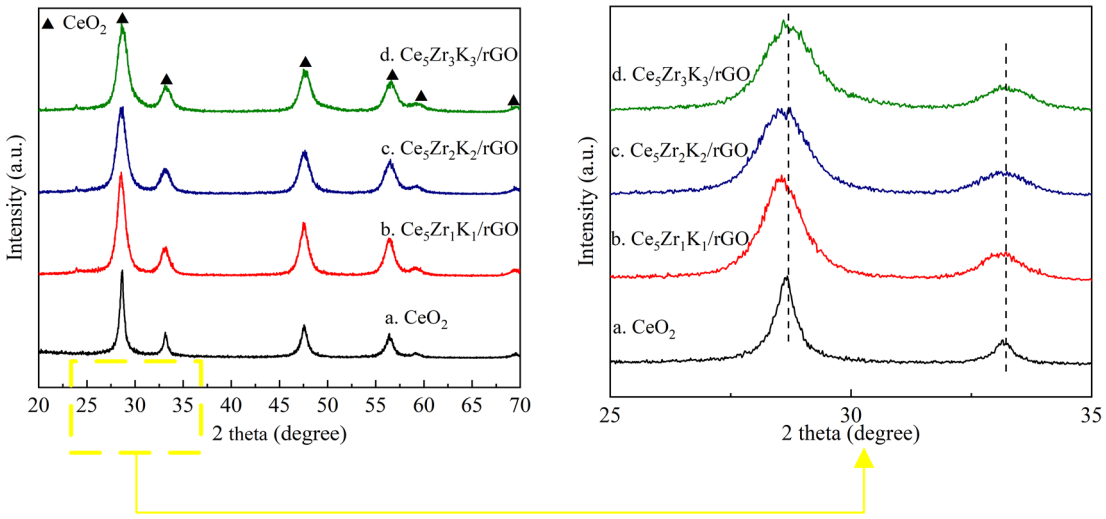

Figure 4. X-ray powder diffraction (XRD) patterns of CeO_2 and $Ce_5Zr_2K_2$/rGO catalysts.

As adsorption and diffusion are the critical processes in a heterogeneous catalytic reaction, the pore structure of the catalyst has a great impact on catalytic performance [32]. Figure 5 displays the N_2 adsorption isotherms and pore size distribution of the as-prepared catalysts. A similar IV type isotherm with H3-type hysteresis loops on IUPAC classification suggested that the CeZrK/rGO catalysts had mesoporous distribution characteristic [33]. From Figure 5b,d,f, it can be seen that the most probable pore size of $Ce_5Zr_1K_1$/rGO, $Ce_5Zr_2K_2$/rGO, and $Ce_5Zr_3K_3$/rGO were 36.9 nm, 36.8 nm, and 36.1 nm, respectively, which were larger than that of soot (>20 nm). At this time, most of the soot particles stayed on the external surface, and some entered the pores, which increased the contact area between the catalyst and the PM to a certain extent, thereby improving the catalytic activity.

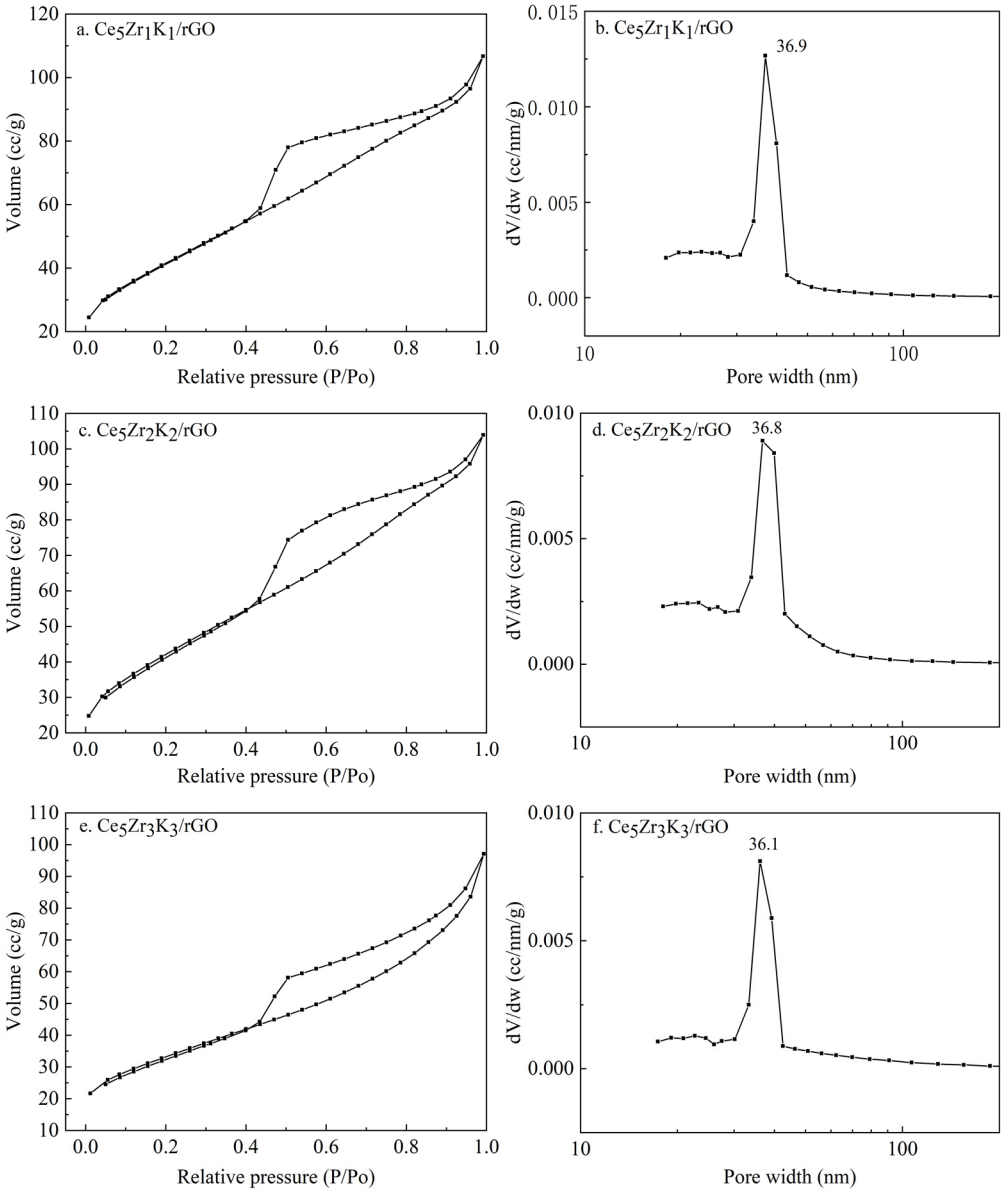

Figure 5. N_2 adsorption isotherms and pore size distributions of CeZrK/rGO catalysts.

Table 1 lists the average crystallite size and the specific surface area (S_{BET}) of the catalysts. The average crystallite sizes was computed from XRD based on the Scherrer equation. The average crystallite size of $Ce_5Zr_1K_1$/rGO, $Ce_5Zr_2K_2$/rGO, and $Ce_5Zr_3K_3$/rGO were 8.3 nm, 6.9 nm, and 6.7 nm, respectively, which were smaller than that of CeO_2 because the lattice distortion caused by the doping of Zr and K ions inhibited the crystal growth of CeO_2 phase [34]. The S_{BET} can be obtained from N_2 adsorption isotherms based on the multi-point BET. The as-prepared catalysts had a higher specific surface area compared to that of CeZrK catalysts (17 m^2/g) in Ref. [35] and other Ce-based catalysts (55–82 m^2/g) in Ref. [36]. Meanwhile, among the CeZrK/rGO catalysts, the specific surface area of $Ce_5Zr_2K_2$/rGO (151.5 m^2/g) and $Ce_5Zr_3K_3$/rGO (152.4 m^2/g) were slightly larger than that of $Ce_5Zr_1K_1$/rGO (117.2 m^2/g). It has proved that graphene-based catalysts have a large surface area and superior pore structure, which effectively guarantees the high catalytic activity of the CeZrK/rGO catalysts [37,38].

Table 1. Average crystallite size and specific surface area of the CeZrK/rGO catalysts.

Catalysts	Average Crystallite Size/nm	$S_{BET}/m^2 \cdot g^{-1}$
$Ce_5Zr_1K_1$	8.3	117.2
$Ce_5Zr_2K_2$	6.9	151.5
$Ce_5Zr_3K_3$	6.7	152.4
CeO_2	8.9	-

Figure 6 presents the Raman profiles of CeZrK/rGO catalysts and GO. The typical Raman peaks of D band and G band appeared around 1350 cm^{-1} and 1594 cm^{-1}, respectively. The D band represents the structural defect caused by oxygen-containing functional groups on the C base, and the G band represents the E_{2g} symmetric mode of sp^2 hybrid C [39]. For the Raman profiles of the CeZrK/rGO catalysts, no bands occurred at 400~500 cm^{-1} assigned to CeO_2 [29], showing good dispersion of the CeO_2 particle on the graphene layers. The intensity ratio of D band to G band (I_D/I_G) is an indicator of disorder degree and the average size of the in-plane sp^2 regions in graphite [39]. The I_D/I_G for $Ce_5Zr_1K_1$/rGO, $Ce_5Zr_2K_2$/rGO, $Ce_5Zr_3K_3$/rGO, and GO were 1.10, 1.28, 1.21, and 0.99, respectively. The higher I_D/I_G means that there may be smaller sp^2 regions and unrepaired defect sites in $Ce_5Zr_2K_2$/rGO. The defect sites on the surface of rGO can efficiently inhibit the agglomeration of metal oxide nanoparticles to reduce the particle size and improve the dispersion characteristics [40], which is consistent with the above results observed in SEM and TEM.

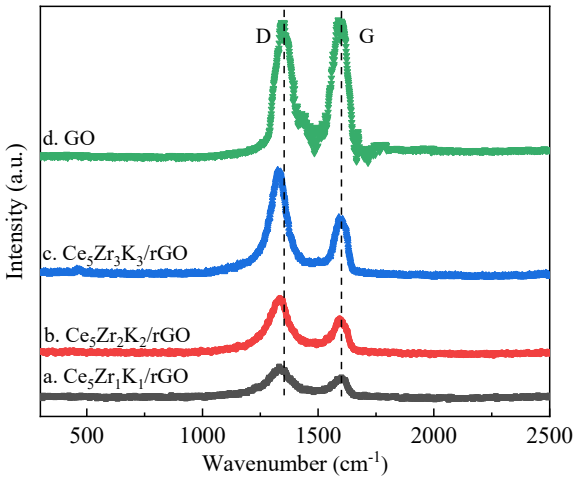

Figure 6. Raman profiles of CeZrK/rGO catalysts and graphene oxide (GO).

The FTIR spectra of CeZrK/rGO catalysts and GO shown in Figure 7 reveals numerous O-containing functional groups such as (O-H) (3423 cm^{-1}) and (C=O) (1735 cm^{-1}) of COOH, (O-H) of tertiary C-OH (1384 cm^{-1}), and (H_2O) (1637 cm^{-1}) [41]. Just on these O-containing groups of GO, during the synthesis of the catalyst, the mixed metal ions (Ce^{4+}, Zr^{4+}, K^+) are first adsorbed uniformly on the surface of negatively charged GO sheets via electrostatic attractions. Compared to GO, the FTIR spectra of CeZrK/rGO catalysts was greatly reduced or even disappeared at 1735 cm^{-1} and 1384 cm^{-1}, implying that GO was deoxidized and reduced to rGO, which was consistent with the phenomenon reported in Ref. [42]. Moreover, the infrared peak changed from 1637 cm^{-1} to 1654 cm^{-1} and 1560 cm^{-1} due to the stretching vibration of C=C. The band at 1228 cm^{-1} emerged from C-O-C stretch epoxy bands on rGO surface.

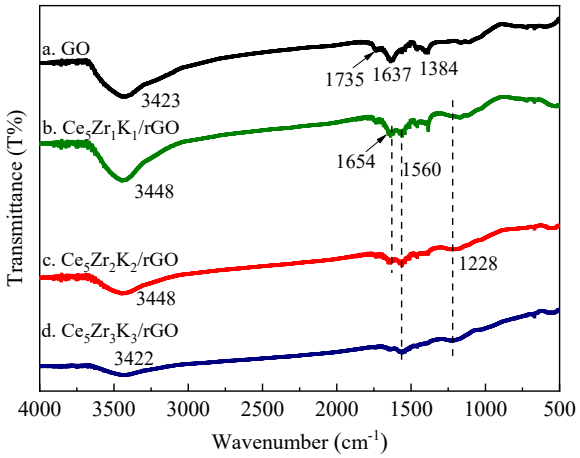

Figure 7. Fourier transform infrared spectrometry (FTIR) spectra of CeZrK/rGO catalysts and GO.

The oxidation states of the main elements Ce, Zr, O and C, including an estimate of the atomic ratio in the CeZrK/rGO catalysts, were achieved using the XPS measurement technique and the corresponding result is depicted in Figure 8. The atomic surface concentrations, the relative percentages, and the binding energy of Ce, Zr, O and C elements in the CeZrK/rGO catalysts are summarized in Tables 2 and 3, respectively. The u and v in the XPS spectra of Ce 3d refer to the $3d_{3/2}$ and $3d_{5/2}$ spin-orbit components, respectively [43]. The peaks of u, u″, u‴ and v, v″, v‴ are attributed to Ce^{4+} ions, whereas u′ and v′ are attributed to Ce^{3+} ions. Therefore, it can be inferred that the CeZrK/rGO catalysts had both Ce^{4+} and Ce^{3+} ions. The Ce^{3+}/Ce^{4+} ratios of the CeZrK/rGO catalysts were calculated by the ratio of the sum of the integrated areas of Ce^{3+} (u′, v′) to the sum of the integrated area of Ce^{4+} (u, v, u″, v″, u‴, v‴) as shown in Table 4. It was found that $Ce_5Zr_2K_2$/rGO exhibits a higher concentration of Ce^{3+} ions, which indicates that $Ce_5Zr_2K_2$/rGO contained more oxygen vacancies [29]. The XPS spectra of Zr 3d in Figure 8b shows that there is no difference in the binding energies of Zr element in the CeZrK/rGO catalysts. The binding energies of Zr $3d_{5/2}$ and Zr $3d_{3/2}$ were 182.6 eV and 185 eV, respectively, which can prove the existence of Zr^{+4} in the CeZrK/rGO catalysts [44]. The XPS spectra of O 1s in Figure 8c presents two types of surface oxygen in the CeZrK/rGO catalysts. The O_I (529.8–530.0 eV) is the characteristic of the surface lattice oxygen (O^{2-}) in cerium oxide, and the O_{II} (531.5-531.8 eV) indicates the presence of chemisorbed oxygen on the surface of oxygen (O^-, O_{2-}, $O_2{}^{2-}$) belonging to the defect-oxygen or hydroxyl-like group [19]. In general, the surface-adsorbed oxygen was derived from the adsorption of gaseous O_2 on the oxygen vacancies of the oxide catalyst. It is clear that $Ce_5Zr_2K_2$/rGO had a much higher O_{II}/O_I peak area ratio than $Ce_5Zr_1K_1$/rGO and $Ce_5Zr_3K_3$/rGO, which effectively increased the concentration of surface-adsorbed oxygen. Compared to the lattice oxygen, chemical adsorbed oxygen (O_{II}) had higher mobility, and thus it played a more important role in the soot oxidation reaction. Figure 8d displays the deconvolution of C 1s peaks in the CeZrK/rGO catalysts. The main peaks are centred in 284.5–284.6 eV, 285.5 eV, and 288.4 eV, which represents graphite structure, C-O, and -O-C=O, respectively. The C-O and -O-C=O bonds in graphene indicate that graphene can provide abundant active sites for the directional connection of CeO_2-ZrO_2 particles. Additionally, the XPS failed to detect the presence of K element. It can be explained that the binding energy of K and C were mainly in the range of 291–296 eV and of 277–295 eV, respectively, and the content of C in the as-prepared catalysts was much larger than that of K, which may have interfered with the detection of K element. Generally, among the three CeZrK/rGO catalysts, the $Ce_5Zr_2K_2$/rGO catalyst contained more oxygen vacancies which is beneficial to improve the OSC of CeO_2, and the $Ce_5Zr_2K_2$/rGO catalyst had a higher chemically adsorbed oxygen concentration.

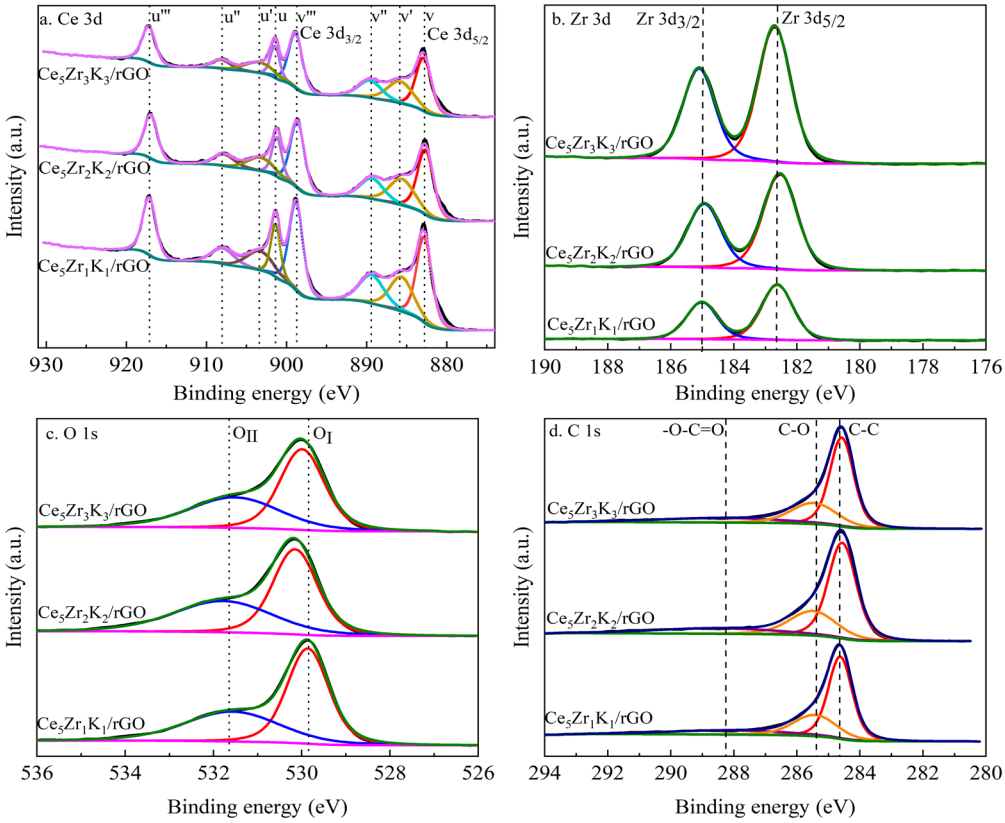

Figure 8. X-ray photoelectron spectroscopy (XPS) spectra for (**a**) Ce 3d, (**b**) Zr 3d, (**c**) O 1s and (**d**) C 1s of the CeZrK/rGO catalysts.

Table 2. Atomic surface composition of CeZrK/rGO catalysts determined from XPS.

Catalysts	Atomic Surface Composition (%)										
	Ce	Zr	O	C	Ce		O		C		
					Ce^{3+}	Ce^{4+}	O_I	O_{II}	C-C	C-O	-O-C=O
$Ce_5Zr_1K_1$/rGO	7.3	1.35	25.96	65.39	61.26	38.74	41.45	58.55	57.35	26.89	15.76
$Ce_5Zr_2K_2$/rGO	4.68	2.11	27.00	66.21	61.83	38.17	40.84	59.16	59.07	25.30	15.62
$Ce_5Zr_3K_3$/rGO	4.47	3.34	24.50	67.68	60.14	39.86	43.51	56.49	59.99	24.78	15.23

Table 3. Binding energies of Ce $3d_{3/2}$ (u'''), Zr $3d_{5/2}$, O_I 1s, and O_{II} 1s of CeZrK/rGO catalysts.

Catalysts	Ce $3d_{3/2}$ (u''')/eV	Zr $3d_{5/2}$/eV	O_I 1s/eV	O_{II} 1s/eV
$Ce_5Zr_1K_1$/rGO	917.3	182.6	529.8	531.6
$Ce_5Zr_2K_2$/rGO	916.9	182.5	530.0	531.8
$Ce_5Zr_3K_3$/rGO	917.0	182.7	529.9	531.5

Table 4. Ce^{3+}/Ce^{4+}, O_{II}/O_I, and Ce/Zr ratios of CeZrK/rGO catalysts.

Catalysts	Ce^{3+}/Ce^{4+}	O_{II}/O_I/	Ce/Zr
$Ce_5Zr_1K_1$/rGO	1.58	1.41	5.4
$Ce_5Zr_2K_2$/rGO	1.62	1.45	2.2
$Ce_5Zr_3K_3$/rGO	1.51	1.30	1.3

Figure 9 shows the result of the H_2-TPR analyses administered on GO and CeZrK/rGO catalysts to examine their redox behavior. It was shown that the reduction peak of GO appears at 663 °C, while no obvious reduction peak was observed for the CeZrK/rGO catalysts at 550–650 °C, indicating that the oxygen-containing functional groups on the

GO surface are deoxidized during the preparation [45], which agrees with the FTIR results shown in Figure 7. Three obvious reduction peaks ranging from 250 °C to 600 °C were observed for the CeZrK/rGO catalysts. The shoulder peak at 360 °C corresponds to adsorbent oxygen, and the reduction peak at 465 °C corresponds to the reduction of the outermost layer of Ce^{4+} to Ce^{3+}. The reduction peak ranging from 700 °C to 850 °C can be attributed to the reduction of CeO_2 (Ce^{4+} inner layer) and the reduction of lattice oxygen (bulk reduction) [46]. Curve b has a higher peak intensity ratio (surface/bulk reduction) than that of other curves, which indicates the enhanced oxygen mobility within the lattice of $Ce_5Zr_2K_2$/rGO. Due to the synergistic effect of Ce and Zr, a shoulder peak occurs around 301 °C. Moreover, the peak at around 465 °C in curve b moves to low temperature, indicating that the reducibility of $Ce_5Zr_2K_2$/rGO improved. The reduction peak in curve c becomes flat due to the aggregation of excess metal oxides, which could impact negatively on the catalytic performance of $Ce_5Zr_3K_3$/rGO. In general, the doping of Zr and K ions into CeO_2 with graphene as the carrier can effectively promoted the formation of a solid solution. The graphene can enhance the redox capacity of cerium oxide at low temperatures [47]. All the CeZrK/rGO catalysts showed a superior redox capacity, and this reflects on the improved catalytic oxidation activity of the soot. Meanwhile, the redox capacity of the CeZrK/rGO catalysts was affected by the metal doping ratio. Among the CeZrK/rGO catalysts, $Ce_5Zr_2K_2$/rGO presents the lowest reduction temperature in the H_2-TPR profiles.

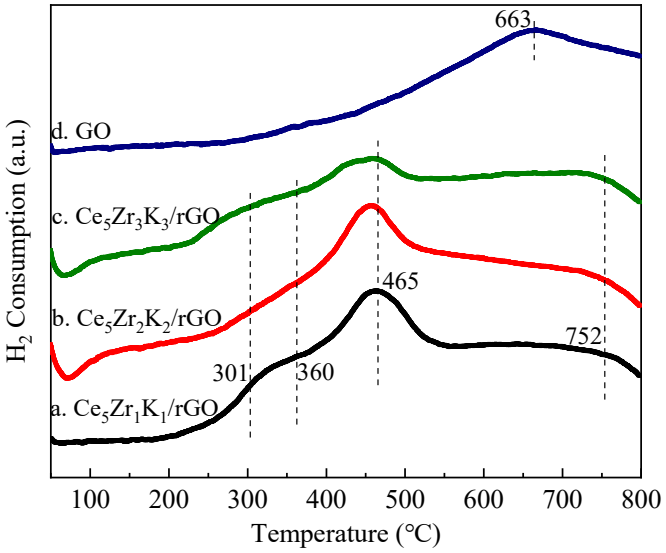

Figure 9. H_2-temperature programmed reduction (H_2-TPR) profiles of GO and CeZrK/rGO catalysts.

3.2. Evaluation on Catalytic Activity for Soot Oxidation

The catalytic activity of the CeZrK/rGO catalysts for soot oxidation were evaluated under the tight contact and loose contact modes in simulated air (21% O_2 + 79% N_2) by thermogravimetric analysis. Figure 10 shows the normalized soot conversion under the tight contact mode as the function of temperature over the as-prepared catalysts. To provide a better comparison for the catalytic activity, T_{50} was defined as the temperature at which 50% soot conversion is achieved and T_m was defined as the temperature at which the maximum rate of soot combustion occurs [48]. The results show that the T_{50} of $Ce_5Zr_1K_1$/rGO, $Ce_5Zr_2K_2$/rGO, $Ce_5Zr_3K_3$/rGO, and CeO_2 were 352 °C, 339 °C, 358 °C, and 407 °C, respectively. It can be inferred that the CeZrK/rGO catalysts had higher catalytic activity than CeO_2. The difference of T_{50} among the CeZrK/rGO catalysts was small due to the tight contact between soot and the catalyst. Under this condition, the difference in the structure and morphology of the CeZrK/rGO catalysts had a small impact on the catalytic activity.

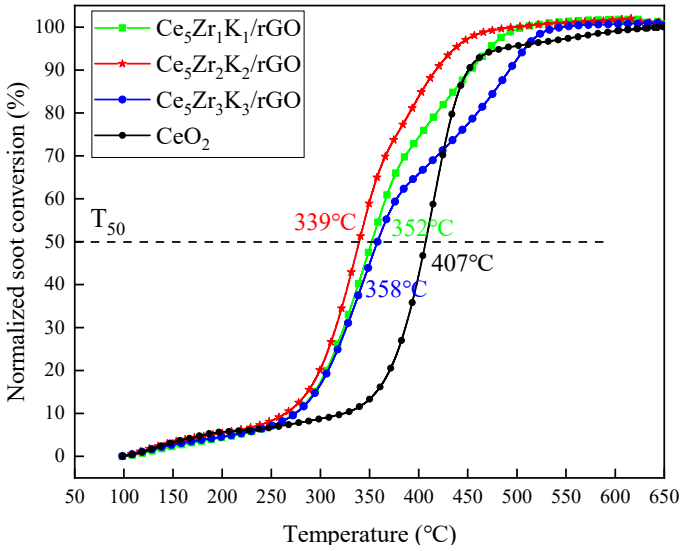

Figure 10. Normalized soot conversion versus temperature of CeZrK/rGO catalysts under tight contact mode in simulated air (21% O_2 + 79% N_2).

The loose contact mode is the most realistic approach because soot is mixed with the catalyst without any force exertion [49]. Figure 11 shows the normalized soot conversion under the loose contact mode as a function of temperature with and without as-prepared catalysts. The T_{50} for $Ce_5Zr_1K_1$/rGO, $Ce_5Zr_2K_2$/rGO, and $Ce_5Zr_3K_3$/rGO were 390 °C, 383 °C, and 432 °C, respectively, which were far less than those of CeO_2 (523 °C), rGO (532 °C) and catalyst-free (604 °C). The catalytic activity of rGO on soot oxidation was presented due to the fact that rGO contains residual structural defects, which improve oxygen reduction reactions. The higher catalytic activity of $Ce_5Zr_2K_2$/rGO was closely related to its superior dispersion quality, small particle size (Figure 2d), large specific surface area (Table 1), and abundant oxygen vacancies (Figure 8 and Table 3) and redox capacity (Figure 9). It should be noted that the slope of the curve before 300 °C was arranged in the order of $Ce_5Zr_3K_3$/rGO > $Ce_5Zr_2K_2$/rGO > $Ce_5Zr_1K_1$/rGO, which is consistent with the order of the specific surface area (Table 1) of the three CeZrK/rGO catalysts. The slope of the curve after 300 °C was arranged in the order of $Ce_5Zr_2K_2$/rGO > $Ce_5Zr_1K_1$/rGO > $Ce_5Zr_3K_3$/rGO, which is consistent with the order of oxygen vacancy concentration (Ce^{3+}/Ce^{4+}) and the concentration of chemically adsorbed oxygen (O_{II}/O_I) (Table 4). This may be due to the fact that the specific surface area had a greater influence on the activity in the low temperature region, while the oxygen vacancy concentration had a greater influence on the activity in the medium and high temperature region. In order to avoid the influence of graphene on experimental data, the weight loss of modified graphene under air atmosphere was investigated. As shown in Figure 12, the weight loss was 2.3 (wt)% and mainly occurred at 520 °C, which had little impact on the TG experimental data.

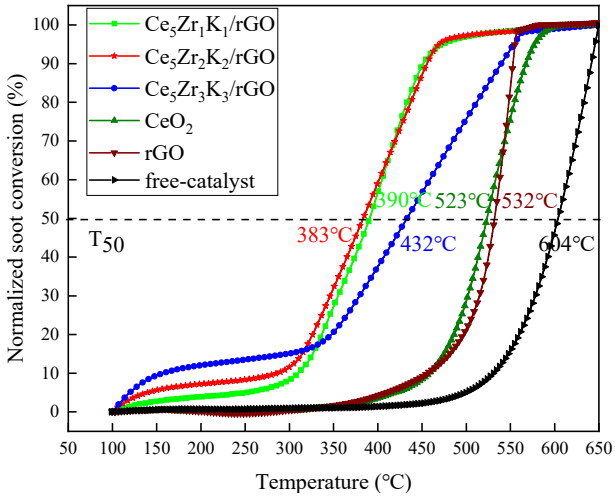

Figure 11. Normalized soot conversion versus temperature of CeZrK/rGO catalysts and free-catalyst under loose contact mode in simulated air (21% O_2 + 79% N_2).

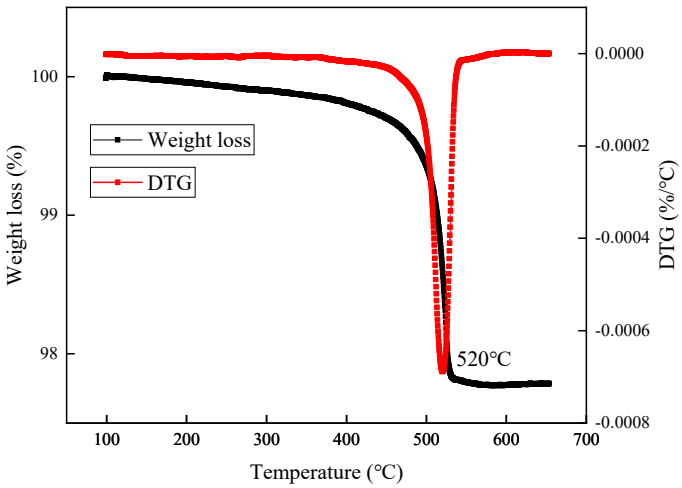

Figure 12. TG/DTG (thermo gravimetric analysis/derivative thermo gravimetric analysis) profiles of $Ce_5Zr_2K_2$/rGO in simulated air (21% O_2 + 79% N_2).

The research on the surface oxygen species is necessary for the catalytic oxidation reaction. Therefore, the catalytic performance of the CeZrK/rGO catalysts in pure N_2 was performed as shown in Figure 13. Due to the absence of gaseous O_2, soot can only be oxidized by active adsorbed oxygen (O^-, O_2^-) and lattice oxygen (O^{2-}) from the catalyst surface. It can be seen from DTG profiles that there was a trough for the CeZrK/rGO catalysts at 318~322 °C, which is attributed to the soot oxidation by adsorbed oxygen. The troughs for $Ce_5Zr_2K_2$/rGO and $Ce_5Zr_3K_3$/rGO at 513 °C and 521 °C, respectively, correspond to the soot oxidation by lattice oxygen. In comparison with the peak strength and the peak temperature, $Ce_5Zr_2K_2$/rGO showed a better catalytic performance among the CeZrK/rGO catalysts, which can be derived from its abundant reactive oxygen species and reasonable metal doping concentration, improving the mobility of adsorbed oxygen and lattice oxygen.

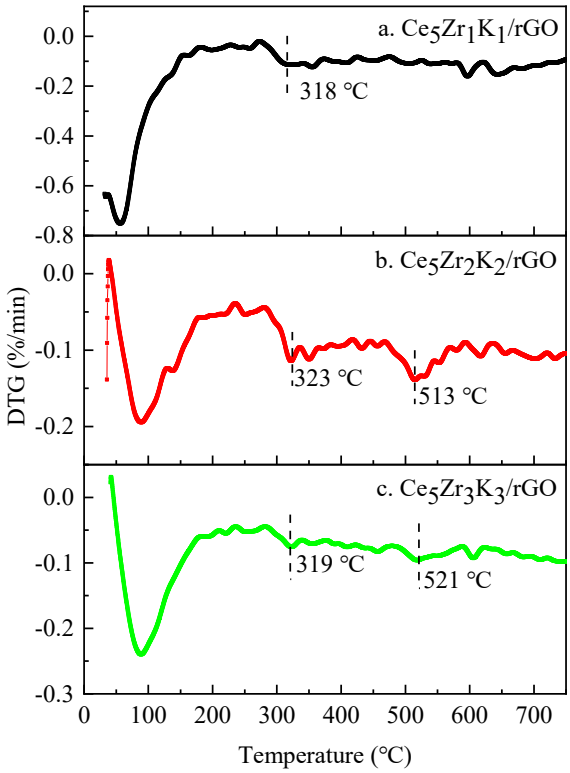

Figure 13. DTG plots of soot combustion in tight contact mode over CeZrK/rGO catalysts in a pure N_2 atmosphere.

Tables 5 and 6 compare the catalytic performance of various catalysts with high catalytic activity, including perovskite catalysts, noble metal catalysts, and CeZrK/rGO catalysts for soot oxidation [9,19,30,50–59]. It is clear that the CeZrK/rGO catalysts by doping metal oxide particles onto graphene have higher catalytic activity than other catalysts, especially for $Ce_5Zr_2K_2$/rGO. Generally, $Ce_5Zr_2K_2$/rGO is a promising catalyst for the catalytic oxidation of soot in the CDPF owing to the advantages of easy synthesis, low cost, and high catalytic activity.

Table 5. T_{50} of various catalysts for soot oxidation under tight contact and loose contact conditions.

Catalyst Name	T_{50} (°C)		Refs.
	Tight	Loose	
Catalyst-free	-	604	This work
CeO_2-Sm_2O_3	417	517	[30]
Pt/Al_2O_3	-	464	[50]
Ag/MnO_x	-	498	[51]
$LaCo_{0.94}Pt_{0.06}O_3$	-	437	[52]
3DOM $La_{0.8}Ce_{0.2}FeO_3$	-	434	[53]
3DOM $LaCo_{0.5}$ $Fe_{0.5}O_3$	-	397	[54]
3DOM $Ce_{0.8}Zr_{0.2}O_2$	-	396	[55]
3DOM $Sr_{0.8}K_{0.2}TiO_3$	-	382	[56]
CeO_2 [a]	419	523	This work
$Ce_5Zr_1K_1$/rGO [a]	352	390	This work
$Ce_5Zr_2K_2$/rGO [a]	339	383	This work
$Ce_5Zr_3K_3$/rGO [a]	358	432	This work

[a] Based on TGA methods at the heating rate of 10 °C/min.

Table 6. T_m of various catalysts for soot oxidation under tight contact and loose contact conditions.

Catalyst Name	T_m (°C)		Refs.
	Tight	Loose	
$Au_{0.08}/LaFeO_3$	-	359	[9]
$Pt_{0.1}Ce_{0.68}Zr_{0.31}$	-	430	[60]
$Pt_{0.1}Al_{0.99}$	-	464	[60]
3DOM $La_{0.95}K_{0.05}NiO_3$	-	341	[57]
$LaNiO_3$	-	431	[61]
CoMgAl-LDH/rGO	433	477	[19]
$Ce_{0.68}Zr_{0.32}O_2$	440	620	[58]
$K_{0.2}Ce_{0.544}Zr_{0.256}O_2$	440	490	[58]
CeZrK mixed oxides	-	445	[35]
CeZrKRu mixed oxides	-	391	[59]
CeO_2	416	588	This work
$Ce_5Zr_1K_1/rGO$	342	347	This work
$Ce_5Zr_2K_2/rGO$	329	344	This work
$Ce_5Zr_3K_3/rGO$	339	330	This work

4. Conclusions

Today the environmental pollution [62–65] and energy crisis [66–68] have to learn another new problem. In this study, a new nanostructured solid solution catalyst CeZrK/rGO was prepared for the catalytic oxidation of soot by loading CeO_2-ZrO_2-K_2O nanoparticles on the surface of rGO. Some major conclusions can be summarized as follows:

1. The use of rGO as the carrier of CeZrK/rGO catalysts provides a large specific surface area and special pore structure, increasing the contact between soot and catalyst compared to the Ce-based catalysts without rGO.
2. The doping of Zr and K ions in the CeZrK/rGO catalysts leads to the lattice distortion of CeO_2, which can increase oxygen vacancies and active oxygen species, control the crystallite growth of CeO_2, and ensure the dispersion quality of active sites.
3. The characterization studies show that the CeZrK/rGO catalysts have nanoscale pore structure, superior dispersion quality, small particle size, large specific surface area, as well as sufficient oxygen vacancies.
4. The T_{50} related to soot conversion of $Ce_5Zr_1K_1/rGO$, $Ce_5Zr_2K_2/rGO$, and $Ce_5Zr_3K_3/rGO$ under tight contact and loose contact conditions were 352 °C, 339 °C, 358 °C and 390 °C, 383 °C, 432 °C, respectively, which are smaller than those of some typical rare earth, perovskite, and precious metal catalysts, such as CeO_2, 3DOM $La_{0.8}Ce_{0.2}FeO_3$, Pt/Al_2O_3, etc. It is indicated that the CeZrK/rGO catalysts have high catalytic activity for soot oxidation, especially for $Ce_5Zr_2K_2/rGO$.

Author Contributions: Conceptualization, Y.L. (Yuqiang Li); methodology, G.W.; investigation, K.T. and D.W.; data curation, K.T. and D.W.; writing—original draft preparation, G.W.; writing—review and ed-iting, Y.L. (Yuelin Li); supervision, Y.L. (Yuqiang Li); project administration, G.W.; funding acquisition, G.W. and Y.L. (Yuqiang Li). All authors have read and agreed to the published version of the manuscript.

Funding: This research was funded by National Natural Science Foundation of China, grant number 51976016, Research Foundation of Education Bureau of Hunan Province, grant number 18B149, Open Research Subject of Key Laboratory of Advanced Manufacture Technology for Automobile Parts, grant number 2017KLMT02.

Institutional Review Board Statement: Not applicable.

Informed Consent Statement: Not applicable.

Data Availability Statement: The data presented in this study are available in the main text of the article.

Conflicts of Interest: The authors declare no conflict of interest.

References

1. Ratcliff, M.A.; Dane, A.J.; Williams, A.; Ireland, J.; Luecke, J.; McCormick, R.L.; Voorhees, K.J. Diesel Particle Filter and Fuel Effects on Heavy-Duty Diesel Engine Emissions. *Environ. Sci. Technol.* **2010**, *44*, 8343. [CrossRef]
2. Wu, G.; Wang, X.; Li, Y.; Liu, Z. A Realistic Skeletal Mechanism for the Oxidation of Biodiesel Surrogate Composed of Long Carbon Chain and Polyunsaturated Compounds. *Fuel* **2021**, *289*, 119934. [CrossRef]
3. Wu, G.; Wu, D.; Li, Y.; Meng, L. Effect of Acetone-n-butanol-ethanol (ABE) as an Oxygenate on Combustion, Performance, and Emission Characteristics of a Spark Ignition Engine. *J. Chem.* **2020**, *2020*, 7468651. [CrossRef]
4. Johnson, T.V. Review of Diesel Emissions and Control. *Int. J. Engine Res.* **2009**, *10*, 275. [CrossRef]
5. Peck, R.; Becker, C. Experimental Investigations and Dynamic Simulation of Diesel Particulate Filter Systems. *Chem. Eng. Technol.* **2009**, *32*, 1411. [CrossRef]
6. Cauda, E.; Fino, D.; Saracco, G.; Specchia, V. Preparation and Regeneration of a Catalytic Diesel Particulate filter. *Chem. Eng. Sci.* **2007**, *62*, 5182. [CrossRef]
7. Shukla, P.C.; Gupta, T.; Labhasetwar, N.K.; Khobaragade, R.; Gupta, N.K.; Agarwal, A.K. Effectiveness of Non-Noble Metal Based Diesel Oxidation Catalysts on Particle Number Emissions from Diesel and Biodiesel Exhaust. *Sci. Total Environ.* **2017**, *574*, 1512. [CrossRef] [PubMed]
8. Mamontov, E.; Brezny, R.; Koranne, M.; Egami, T. Nanoscale Heterogeneities and Oxygen Storage Capacity of $Ce_{0.5}Zr_{0.5}O_2$. *J. Phys. Chem. B.* **2003**, *107*, 13007. [CrossRef]
9. Wei, Y.; Liu, J.; Zhao, Z.; Chen, Y.; Xu, C.; Duan, A.; Jiang, G.; He, H. Highly Active Catalysts of Gold Nanoparticles Supported on Three-Dimensionally Ordered Macroporous $LaFeO_3$ for Soot Oxidation. *Angew. Chem. Int. Ed.* **2011**, *50*, 2326. [CrossRef]
10. Da, Y.; Zeng, L.; Wang, C.; Mao, T.; Chen, R.; Gong, C.; Fan, G. Catalytic oxidation of diesel soot particulates over Pt substituted $LaMn_{1-x}Pt_xO_3$ perovskite oxides. *Catal. Today* **2019**, *327*, 73. [CrossRef]
11. Sun, J.; Zhao, Z.; Li, Y.; Yu, X.; Zhao, L.; Li, J.; Wei, Y.; Liu, J. Synthesis and Catalytic Performance of Macroporous $La_{1-x}Ce_xCoO_3$ Perovskite Oxide Catalysts with High Oxygen Mobility for Catalytic Combustion of Soot. *J. Rare Earths* **2020**, *38*, 584. [CrossRef]
12. Mukherjee, D.; Reddy, B.M. Noble Metal-Free CeO_2-Based Mixed Oxides for CO and Soot Oxidation. *Catal. Today* **2018**, *309*, 227. [CrossRef]
13. Atribak, I.; Bueno-López, A.; García-García, A. Combined Removal of Diesel Soot Particulates and NO_x Over CeO_2–ZrO_2 Mixed Oxides. *J. Catal.* **2008**, *259*, 123. [CrossRef]
14. Gross, M.S.; Ulla, M.A.; Querini, C.A. Catalytic Oxidation of Diesel Soot: New Characterization and Kinetic Evidence Related to the Reaction Mechanism on K/CeO_2 catalyst. *Appl. Catal. A* **2009**, *360*, 81. [CrossRef]
15. Tan, L.; Wang, Y.; Liu, Q.; Wang, J.; Jing, X.; Liu, L.; Liu, J.; Song, D. Enhanced Adsorption of Uranium (VI) Using a Three-Dimensional Layered Double Hydroxide/Graphene Hybrid Material. *Chem. Eng. J.* **2015**, *259*, 752. [CrossRef]
16. Mei, X.; Yan, Q.; Lu, P.; Wang, J.; Cui, Y.; Nie, Y.; Umar, A.; Wang, Q. Synthesis of Pt/K_2CO_3/MgAlOx–reduced Graphene Oxide Hybrids as Promising NO_x Storage–Reduction Catalysts with Superior Catalytic Performance. *Sci. Rep.* **2017**, *7*, 42862. [CrossRef]
17. Pan, M.; Qian, W.; Wei, H.; Feng, D.; Pan, J. Effects on Performance and Emissions of Gasoline Compression Ignition Engine over a Wide Range of Internal Exhaust Gas Recirculation Rates under Lean Conditions. *Fuel* **2020**, *265*, 116881. [CrossRef]
18. Wang, P.; Yi, J.; Sun, C.; Luo, P.; Lei, L. Evaluation of H_2 on the Evolution Mechanism of NOx Storage and Reduction over Pt-Ba-Ce/γ-Al2O3 Catalysts. *Engineering* **2019**, *5*, 568. [CrossRef]
19. Pan, M.; Huang, R.; Liao, J.; Ouyang, T.; Lv, D.; Huang, H. Effect of EGR dilution on Combustion, Performance and Emission Characteristics of a Diesel Engine Fueled with n-Pentanol and 2-Ethylhexyl Nitrate Additive. *Energy. Conv. Manag.* **2018**, *176*, 246. [CrossRef]
20. Zhang, P.; Yang, B.; Ma, H.; Wu, Z. Graphene Modified Porous Organic Polymer Supported Phosphotungstic Acid Catalyst for Alkylation Desulfurization. *Fuel* **2021**, *293*, 120438. [CrossRef]
21. Li, X.; Wang, Z.; Wu, L.; Tsai, T. One-step in Situ Synthesis of a Novel α-zirconium Phosphate/Graphene Oxide Hybrid and its Application in Phenolic Foam with Enhanced Mechanical Strength, Flame Retardancy and Thermal Stability. *RSC Adv.* **2016**, *6*, 74903. [CrossRef]
22. Wu, Z.S.; Ren, W.; Gao, L.; Zhao, J.; Chen, Z.; Liu, B.; Tang, D.; Yu, B.; Jiang, C.; Cheng, H.M. Synthesis of Graphene Sheets with High Electrical Conductivity and Good Thermal Stability by Hydrogen Arc Discharge Exfoliation. *ACS Nano* **2009**, *3*, 411. [CrossRef]
23. Bora, C.; Bharali, P.; Baglari, S.; Dolui, S.K.; Konwar, B.K. Strong and Conductive Reduced Graphene Oxide/Polyester Resin Composite Films with Improved Mechanical Strength, Thermal Stability and its Antibacterial Activity. *Compos. Sci. Technol.* **2013**, *87*, 1. [CrossRef]
24. Yuan, B.; Song, L.; Liew, K.M.; Hu, Y. Solid Acid-Reduced Graphene Oxide Nanohybrid for Enhancing Thermal Stability, Mechanical Property and Flame Retardancy of Polypropylene. *RSC Adv.* **2015**, *5*, 41307. [CrossRef]
25. Zong, M.; Huang, Y.; Zhao, Y.; Sun, X.; Qu, C.; Luo, D.; Zheng, J. Facile Preparation, High Microwave Absorption and Microwave Absorbing Mechanism of RGO–Fe_3O_4 Composites. *RSC Adv.* **2013**, *3*, 23638. [CrossRef]
26. Khira, Z.; Nasr, S.; Dorra, J.; Karima, H. Investigations on electrical conductivity and dielectric properties ofgraphene oxide nanosheets synthetized from modified Hummer's method. *J. Mol. Struct.* **2020**, *1216*, 128304.
27. Xiao, Q.; Sun, Y.; Zhang, J.; Li, Q. Size-dependent of Chromium (VI) Adsorption on Nano α-Fe_2O_3 Surface. *Appl. Surf. Sci.* **2015**, *356*, 18. [CrossRef]

28. Sajeevan, A.C.; Sajith, V. Synthesis of Stable Cerium Zirconium Oxide Nanoparticle—Diesel Suspension and Investigation of its Effects on Diesel Properties and Smoke. *Fuel* **2016**, *183*, 155. [CrossRef]
29. Lian, P.; Zhu, X.; Liang, S.; Li, Z.; Yang, W.; Wang, H. High Reversible Capacity of SnO_2/graphene Nanocomposite as an Anode Material for Lithium-Ion Batteries. *Electrochim. Acta* **2011**, *56*, 4532. [CrossRef]
30. Rangaswamy, A.; Sudarsanam, P.; Reddy, B.M. Rare Earth Metal Doped CeO_2-based Catalytic Materials for Diesel Soot Oxidation at Lower Temperatures. *J. Rare Earths* **2015**, *33*, 1162. [CrossRef]
31. You, X.; Sheng, Z.; Yu, D.; Yang, L.; Xiao, X.; Wang, S. Influence of Mn/Ce ratio on the Physicochemical Properties and Catalytic Performance of Graphene Supported MnO_x-CeO_2 Oxides for NH_3-SCR at Low Temperature. *Appl. Surf. Sci.* **2017**, *423*, 845. [CrossRef]
32. Julkapli, N.M.; Bagheri, S. Graphene Supported Heterogeneous Catalysts: An Overview. *Int. J. Hydrog. Energy* **2015**, *40*, 948–979. [CrossRef]
33. Thommes, M.; Kaneko, K.; Neimark, A.V.; Olivier, J.P.; Rodriguez-Reinoso, F.; Rouquerol, J.; Sing, K.S. Physisorption of Gases, with Special Reference to the Evaluation of Surface Area and Pore Size Distribution (IUPAC Technical Report). *Pure Appl. Chem.* **2015**, *87*, 1051. [CrossRef]
34. Shi, Z.M.; Jin, L.N. Influence of La^{3+}/Ce^{3+}-doping on Phase Transformation and Crystal Growth in TiO_2-15wt% ZnO Gels. *J. Non-Cryst. Solids* **2009**, *355*, 213. [CrossRef]
35. Weng, D.; Li, J.; Wu, X.; Si, Z. Modification of CeO_2-ZrO_2 Catalyst by Potassium for NO_x-Assisted Soot Oxidation. *J. Environ. Sci.* **2011**, *23*, 145. [CrossRef]
36. Wei, Y.; Zhao, Z.; Jiao, J.; Liu, J.; Duan, A.; Jiang, G. Preparation of Ultrafine Ce-based Oxide Nanoparticles and Their Catalytic Performances for Diesel Soot Combustion. *J. Rare Earths* **2014**, *32*, 124. [CrossRef]
37. Zheng, C.; Zhou, X.; Cao, H.; Wang, G.; Liu, Z. Synthesis of Porous Graphene/Activated Carbon Composite with High Packing Density and Large Specific Surface Area for Supercapacitor Electrode Material. *J. Power Sources* **2014**, *258*, 290. [CrossRef]
38. Zhang, L.; Zhang, F.; Yang, X.; Long, G.; Wu, Y.; Zhang, T.; Leng, K.; Huang, Y.; Ma, Y.; Yu, A.; et al. Porous 3D Graphene-Based Bulk Materials with Exceptional High Surface Area and Excellent Conductivity for Supercapacitors. *Sci. Rep.* **2013**, *3*, 1408. [CrossRef]
39. Vallés, C.; Núñez, J.D.; Benito, A.M.; Maser, W.K. Flexible Conductive Graphene Paper Obtained by Direct and Gentle Annealing of Graphene Oxide Paper. *Carbon* **2012**, *50*, 835. [CrossRef]
40. Xie, R.; Fan, G.; Ma, Q.; Yang, L.; Li, F. Facile Synthesis and Enhanced Catalytic Performance of Graphene-Supported Ni Nanocatalyst from a Layered Double Hydroxide-Based Composite Precursor. *J. Mater. Chem. A.* **2014**, *2*, 7880. [CrossRef]
41. Strankowski, M.; Włodarczyk, D.; Piszczyk, Ł.; Strankowska, J. Polyurethane Nanocomposites Containing Reduced Graphene Oxide, FTIR, Raman, and XRD Studies. *J. Spectrosc.* **2016**, *2016*, 7520741. [CrossRef]
42. Fan, X.; Peng, W.; Li, Y.; Li, X.; Wang, S.; Zhang, G.; Zhang, F. Deoxygenation of Exfoliated Graphite Oxide under Alkaline Conditions: A Green Route to Graphene Preparation. *Adv. Mater.* **2008**, *20*, 4490. [CrossRef]
43. Larachi, F.; Pierre, J.; Adnot, A.; Bernis, A. Ce 3d XPS Study of Composite $Ce_xMn_{1-x}O_{2-y}$ Wet Oxidation Catalysts. *Appl. Surf. Sci.* **2002**, *195*, 236. [CrossRef]
44. Atiqullah, M.; Akhtar, M.N.; Faiz, M.; Moman, A.; Abu-Raqabah, A.H.; Khan, J.H.; Wazeer, M.I. Surface Chemistry of Selected Supported Metallocene Catalysts Studied by DR-FTIR, CPMAS NMR, and XPS Techniques. *Surf. Interface Anal.* **2006**, *38*, 1319. [CrossRef]
45. Hajjar, Z.; Kazemeini, M.; Rashidi, A.; Bazmi, M. In Situ and Simultaneous Synthesis of a Novel Graphene-Based Catalyst for Deep Hydrodesulfurization of Naphtha. *Catal. Lett.* **2015**, *145*, 1660. [CrossRef]
46. Li, H.; Lu, G.; Dai, Q.; Wang, Y.; Guo, Y.; Guo, Y. Efficient Low-Temperature Catalytic Combustion of Trichloroethylene over Flower-Like Mesoporous Mn-doped CeO_2 Microspheres. *Appl. Catal. B* **2011**, *102*, 475. [CrossRef]
47. Jiao, J.Z.; Li, S.H.; Huang, B.C. Preparation of Manganese Oxides Supported on Graphene Catalysts and their Activity in Low-Temperature NH_3-SCR. *Acta Phys. Chim. Sin.* **2015**, *31*, 1383.
48. Krishna, K.; Bueno-López, A.; Makkee, M.; Moulijn, J.A. Potential Rare Earth Modified CeO_2 Catalysts for Soot Oxidation: I. Characterisation and Catalytic Activity with O_2. *Appl. Catal. B* **2007**, *75*, 189. [CrossRef]
49. Sui, L.; Yu, L. Diesel Soot Oxidation Catalyzed by Co-Ba-K Catalysts: Evaluation of the Performance of the Catalysts. *Chem. Eng. J.* **2008**, *142*, 327. [CrossRef]
50. Liu, S.; Wu, X.; Weng, D.; Li, M.; Fan, J. Sulfation of Pt/Al_2O_3 Catalyst for Soot Oxidation: High Utilization of NO_2 and Oxidation of Surface Oxygenated Complexes. *Appl. Catal. B* **2013**, *138*, 199. [CrossRef]
51. Guilhaume, N.; Bassou, B.; Bergeret, G.; Bianchi, D.; Bosselet, F.; Desmartin-Chomel, A.; Jouguet, B.; Mirodatos, C. In situ Investigation of Diesel Soot Combustion Over an $AgMnO_x$ Catalyst. *Appl. Catal. B* **2012**, *119*, 287. [CrossRef]
52. Zeng, L.; Cui, L.; Wang, C.; Guo, W.; Gong, C. In-situ Modified the Surface of Pt-Doped Perovskite Catalyst for Soot Oxidation. *J. Hazard. Mater.* **2020**, *383*, 121210. [CrossRef] [PubMed]
53. Feng, N.; Chen, C.; Meng, J.; Liu, G.; Fang, F.; Wang, L.; Wan, H.; Guan, G. K–Mn Supported on Three-Dimensionally Ordered Macroporous $La_{0.8}Ce_{0.2}FeO_3$ Catalysts for the Catalytic Combustion of Soot. *Appl. Surf. Sci.* **2017**, *399*, 114. [CrossRef]
54. Xu, J.; Liu, J.; Zhao, Z.; Zheng, J.; Zhang, G.; Duan, A.; Jiang, G. Three-Dimensionally Ordered Macroporous $LaCo_xFe_{1-x}O_3$ Perovskite-Type Complex Oxide Catalysts for Diesel Soot Combustion. *Catal. Today* **2010**, *153*, 136. [CrossRef]

55. Zhang, G.; Zhao, Z.; Liu, J.; Jiang, G.; Duan, A.; Zheng, J.; Chen, S.; Zhou, R. Three Dimensionally Ordered Macroporous $Ce_{1-x}Zr_xO_2$ Solid Solutions for Diesel Soot Combustion. *Chem. Commun.* **2010**, *46*, 457. [CrossRef]
56. Zhao, P.; Feng, N.; Fang, F.; Liu, G.; Chen, L.; Meng, J.; Chen, C.; Wang, L.; Wan, H.; Guan, G. Facile Synthesis of Three-Dimensional Ordered Macroporous $Sr_{1-x}K_xTiO_3$ Perovskites with Enhanced Catalytic Activity for Soot Combustion. *Catal. Sci. Technol.* **2018**, *8*, 5462. [CrossRef]
57. Mei, X.; Xiong, J.; Wei, Y.; Wang, C.; Wu, Q.; Zhao, Z.; Liu, J. Three-Dimensional Ordered Macroporous Perovskite-Type $La_{1-x}K_xNiO_3$ Catalysts with Enhanced Catalytic Activity for Soot Combustion: The Effect of K-Substitution. *Chin. J. Catal.* **2019**, *40*, 722. [CrossRef]
58. Alinezhadchamazketi, A.; Khodadadi, A.A.; Mortazavi, Y.; Nemati, A. Catalytic Evaluation of Promoted CeO_2-ZrO_2 by Transition, Alkali, and Alkaline-Earth Metal Oxides for Diesel Soot Oxidation. *J. Environ. Sci.* **2013**, *25*, 2498. [CrossRef]
59. Matarrese, R.; Morandi, S.; Castoldi, L.; Villa, P.; Lietti, L. Removal of NO_x and Soot Over Ce/Zr/K/Me (Me = Fe, Pt, Ru, Au) Oxide Catalysts. *Appl. Catal. B* **2017**, *201*, 318. [CrossRef]
60. Liu, S.; Wu, X.; Lin, Y.; Li, M.; Weng, D. Active Oxygen-Assisted NO-NO_2 Recycling and Decomposition of Surface Oxygenated Species on Diesel Soot with $Pt/Ce_{0.6}Zr_{0.4}O_2$ Catalyst. *Chin. J. Catal.* **2014**, *35*, 407. [CrossRef]
61. Wang, H.; Zhao, Z.; Xu, C.; Duan, A.; Liu, J.; Chi, Y. Simultaneous Removal of Soot Particles and NO From Diesel Engines Over $LaBO_3$ Perovskite-Type Oxides. *J. Phys. Chem.* **2008**, *29*, 649.
62. Han, D.; E, J.; Deng, Y.; Chen, J.; Leng, E.; Liao, G.; Zhao, X.; Feng, C.; Zhang, F. A review of studies using hydrocarbon adsorption material for reducing hydrocarbon emissions from cold start of gasoline engine. *Renew. Sustain. Energy Rev.* **2021**, *135*, 110079. [CrossRef]
63. Zhao, X.; E, J.; Liao, G.; Zhang, F.; Chen, J.; Deng, Y. Numerical simulation study on soot continuous regeneration combustion model of diesel particulate filter under exhaust gas heavy load. *Fuel* **2021**, *287*, 119795. [CrossRef]
64. E, J.; Zhao, M.; Zuo, Q.; Zhang, B.; Zhang, Z.; Peng, Q.; Han, D.; Zhao, X.; Deng, Y. Effects analysis on diesel soot continuous regeneration performance of a rotary microwave-assisted regeneration diesel particulate filter. *Fuel* **2020**, *260*, 116353. [CrossRef]
65. Zhang, Z.; Ye, J.; Tan, D.; Feng, Z.; Luo, J.; Tan, Y.; Huang, Y. The effects of Fe_2O_3 based DOC and SCR catalyst on the combustion and emission characteristics of a diesel engine fueled with biodiesel. *Fuel* **2021**, *290*, 120039. [CrossRef]
66. Wei, K.; Yang, Y.; Hong, Y.; Zhong, D. A review on ice detection technology and ice elimination technology for wind turbine. *Wind Energy* **2019**, *23*, 433–457. [CrossRef]
67. Zuo, H.; Liu, G.; E, J.; Zuo, W.; Wei, K.; Hu, W.; Tan, J.; Zhong, D. Catastrophic analysis on the stability of a large dish solar thermal power generation system with wind-induced vibration. *Sol. Energy* **2019**, *183*, 40–49. [CrossRef]
68. Zuo, H.; Tan, J.; Wei, K.; Huang, Z.; Zhong, D.; Xie, F. Effects of different poses and wind speeds on wind-induced vibration characteristics of a dish solar concentrator system. *Renew. Energy* **2021**, *168*, 1308–1326. [CrossRef]